Available online at www.sciencedirect.com
ScienceDirect
Journal of Power Sources 170 (2007) 476–489
JOURNAL OF POWER SOURCES
www.elsevier.com/locate/jpowsour

A three-dimensional thermal abuse model for lithium-ion cells

Gi-Heon Kim [a,*], Ahmad Pesaran [a], Robert Spotnitz [b]

[a] *National Renewable Energy Laboratory, 1617 Cole Boulevard, Golden, CO 80401, USA*
[b] *Battery Design LLC, 2277 DeLucchi Drive, Pleasanton, CA 94588, USA*

Received 16 February 2007; received in revised form 28 March 2007; accepted 3 April 2007
Available online 18 April 2007

Abstract

To understand further the thermal abuse behavior of large format Li-ion batteries for automotive applications, the one-dimensional modeling approach formulated by Hatchard et al. [T.D. Hatchard, D.D. MacNeil, A. Basu, J.R. Dahn, J. Electrochem. Soc. 148(7) (2001) A755–A761] was reproduced. Then it was extended to three dimensions so we could consider the geometrical features, which are critical in large cells for automotive applications. The three-dimensional model captures the shapes and dimensions of cell components and the spatial distributions of materials and temperatures, and is used to simulate oven tests, and to determine how a local hot spot can propagate through the cell. In simulations of oven abuse testing of cells with cobalt oxide cathode and graphite anode with standard $LiPF_6$ electrolyte, the three-dimensional model predicts that thermal runaway will occur sooner or later than the lumped model, depending on the size of the cell. The model results showed that smaller cells reject heat faster than larger cells; this may prevent them from going into thermal runaway under identical abuse conditions. In simulations of local hot spots inside a large cylindrical cell, the three-dimensional model predicts that the reactions initially propagate in the azimuthal and longitudinal directions to form a hollow cylinder-shaped reaction zone.

Keywords: Li-ion battery; Thermal runaway; Abuse modeling; Battery modeling; Hybrid electric vehicle

1. Introduction

Small lithium-ion (Li-ion) cells and multistring battery packs are now commonly used in consumer products. Larger packs (>200 Wh) are limited to niche applications like satellites, in large part because of safety concerns. With increasing interest in large-format Li-ion batteries for automotive applications, we need to better understand the abuse tolerance of these batteries.

Li-ion batteries present an attractive energy storage device for electric vehicles (EVs) and hybrid electric vehicles (HEVs) for several reasons. The high cost of nickel may give Li-ion batteries a cost advantage over nickel/metal-hydride (Ni/MH) batteries. Ni/MH cells, which are widely used in HEVs, have a voltage of about 1.2 V, whereas Li-ion cells typically have a voltage of about 3.6 V. So the same system voltage can be achieved with one-third the number of Li-ion cells as Ni/MH cells. Reducing the number of cells dramatically increases reliability because the cells are usually connected in series. Thus, the failure of a single cell could deactivate an entire module. Li-ion cells have up to twice the gravimetric energy density and two to three times the gravimetric power density of Ni/MH cells, which improve the energy efficiency of HEVs. Plug-in hybrid electric vehicle (PHEV) or EV applications, which require higher energy/power battery systems, may benefit even more. Lastly, recent evidence suggests that Li-ion batteries have the potential of achieving better low-temperature performance than Ni/MH batteries. These advantages make Li-ion an attractive candidate for advanced automotive energy storage systems, but adoption of the technology is delayed by problems of cost, life, low-temperature performance, and abuse tolerance.

Abuse tolerance is an especially daunting problem as it relates to safety issues. Acceptable abuse tolerance in small consumer Li-ion cells (<3 Ah) and packs (<150 Wh) has been achieved by the generous (and often redundant) use of safety devices (such as shutdown separator, positive temperature coefficient [PTC], current interrupt, electronic, and pressure vent devices) [1,2].

However, achieving good abuse tolerance with the larger Li-ion cells (>6 Ah) and packs (>200 Wh) needed for automotive applications remains challenging. The high-power requirements

* Corresponding author. Tel.: +1 303 275 4437; fax: +1 303 275 4415.
E-mail addresses: Gi_Heon_Kim@nrel.gov (G.-H. Kim), ahmad_pesaran@nrel.gov (A. Pesaran), rspotnitz@batdesign.com (R. Spotnitz).

0378-7753/$ – see front matter © 2007 Elsevier B.V. All rights reserved.
doi:10.1016/j.jpowsour.2007.04.018

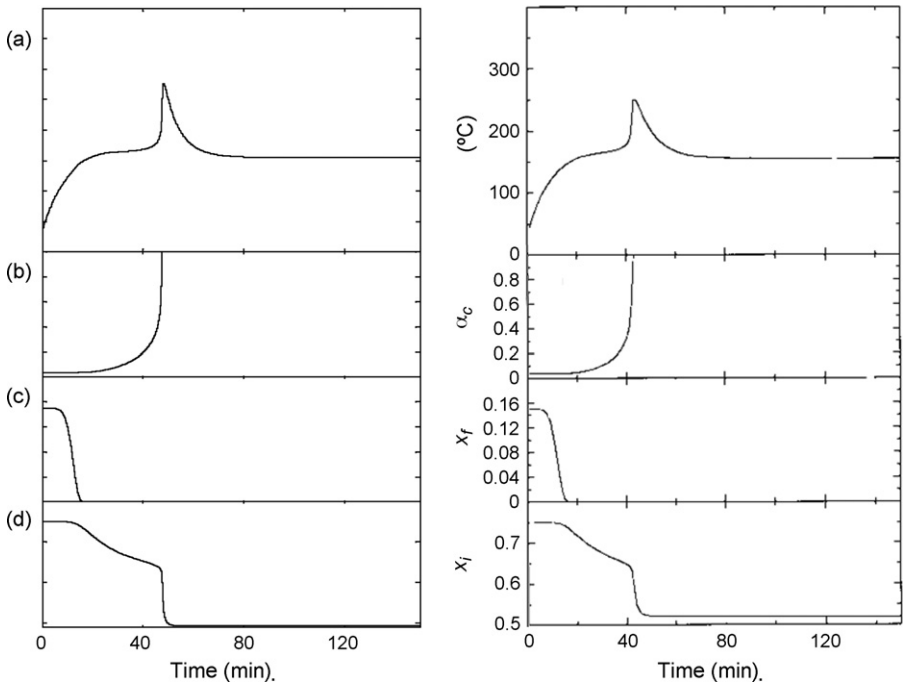

Fig. 1. Comparison of chemistry box model for three-dimensional model with results of Hatchard et al. [5] for oven heating (155 °C) of $LiCoO_2$/graphite 18650 cell. Figure at left is from the box model for three-dimensional model developed here and figure at right is taken from Hatchard.

of the HEV/PHEV/EV applications prevent the use of PTC and other safety devices. Larger cells are intrinsically more vulnerable to thermal runaway because they have higher energy content. Increasing cell size lowers the surface:volume ratio, which in turn reduces cooling area per volumetric heat generation. In addition, increasing the size of a cell increases the temperature difference inside a cell for two reasons: higher heat flux caused by smaller surface:volume ratio, and higher thermal resistance caused by a larger heat diffusion distance. A wider cell temperature distribution for a given surface heat transfer condition

Table 1
Physical and kinetic parameters used for abuse simulations

Symbol	Description	Value	Refs.
A_{sei}	SEI-decomposition frequency factor	1.667E15 (s^{-1})	[5]
A_{ne}	Negative-solvent frequency factor	2.5E13 (s^{-1})	[5]
A_{pe}	Positive-solvent frequency factor	6.667E13 (s^{-1})	[5]
A_e	Electrolyte decomposition frequency factor	5.14E25 (s^{-1})	[6]
$E_{a,sei}$	SEI-decomposition activation energy	1.3508E5 (J mol^{-1})	[5]
$E_{a,ne}$	Negative-solvent activation energy	13508E5 (J mol^{-1})	[5]
$E_{a,pe}$	Positive-solvent activation energy	1396E5 (J mol^{-1})	
$E_{a,e}$	Electrolyte decomposition activation energy	2.74E5 (J mol^{-1})	[6]
c_{sei0}	Initial value of c_{sei}	0.15	[5]
c_{neg0}	Initial value of c_{neg}	0.75	[5]
α_0	Initial value of α	0.04	[5]
c_{e0}	Initial value of c_e	1	[5]
m_{sei}	Reaction order for c_{sei} (Eq. (7))	1	[5]
$m_{ne,n}$	Reaction order for c_{neg} (Eqs. (10)–(11))	1	[5]
$m_{pe,p1}$	Reaction order for α (Eq. (14))	1	[5]
$m_{pe,p2}$	Reaction order for $(1-\alpha)$ (Eq. (14))	1	[5]
m_e	Reaction order for c_e (Eq. (17))	1	
t_{sei0}	Initial value of t_{sei}	0.033	[5]
H_{sei}	SEI-decomposition heat release	257 (J g^{-1})	[5,6]
H_{ne}	Negative-solvent heat release	1714 (J g^{-1})	[5,6]
H_{pe}	Positive-solvent heat release	314 (J g^{-1})	[5,6]
H_{ele}	Electrolyte decomposition heat release	155 (J g^{-1})	[6,20]
W_c	Specific carbon content in jellyroll	6.104E5 (g m^{-3})	
W_p	Specific positive active content in jellyroll	1.221E6 (g m^{-3})	
W_e	Specific electrolyte content in jellyroll	4.069E5 (g m^{-3})	
$\rho c_{p,jr}$	Volumetric heat capacity of jellyroll	2.789E6 (J m^{-3} K^{-1})	

raises the possibility of local onset temperatures that trigger cell thermal runaway.

A more comprehensive understanding about the thermal behaviors of Li-ion batteries at elevated temperatures is required to design a large, abuse-tolerant cell. The U.S. Department of Energy is supporting research and development at national laboratories (ATD and BATT Programs) and FreedomCAR battery developers (U.S. Advanced Battery Consortium Programs) to investigate methods and materials that address the abuse tolerance of Li-ion cells and packs. The development of small, abuse-tolerant Li-ion cells for consumer use relies heavily on "build and break" cycles. For example, shutdown separator specifications were developed and verified based on abuse testing large numbers of cells. However, for large automotive cells, this trial-and-error design process does not seem viable, because it is expensive and time-consuming for large cells; moreover, the build and break test would provide only limited information for effectively improving the abuse tolerance of the cells.

The objectives of this study are to provide better insight about the behaviors of cells under abuse conditions by developing a three-dimensional thermal abuse model for Li-ion batteries, and to accelerate the development of abuse-tolerant Li-ion batteries for vehicle applications by establishing a tool and methodology to support the design.

2. Model development

Designing large Li-ion batteries has raised questions such as: How do the cell sizes and shapes affect abuse tolerance? How important is heat transfer from the tabs to good abuse tolerance? Are shutdown separators effective in large cells? If so, what is the optimal temperature for onset of shutdown? Will thermal runaway propagate to other cells? Under which scenarios? What are the safety margins for key design parameters?

A multidisciplinary science and engineering approach is required to understand the issues of Li-ion battery abuse behaviors, which are related to the various aspects from material properties to assembly methods. However, the key to resolving the abuse tolerance problem in Li-ion batteries lies in thermal engineering—controlling the heat generation and the internal and external heat transfer.

Researchers have tried to model the abuse reactions that occur in Li-ion batteries [3–8]. Hallaj et al. [8] developed a one-dimensional thermal model and identified conditions under which large cells could go into thermal runaway. Botte et al. [3] modified a DUAL model [9] by adding a term to the energy balance to account for an exothermic chemical reaction at the negative; they found that the chemical reaction of the negative was negligible under normal conditions. Richard and Dahn [10] showed how accelerating rate calorimetry (ARC) studies of small samples could be used to predict oven abuse results for full cells. Hatchard et al. [4] showed the importance of considering radiative heat transfer in oven abuse testing. Hatchard et al. [5] later presented a model for predicting oven abuse tests based on expressions for the exotherms of the electrodes obtained by ARC and differential scanning calorimetry studies. This approach was extended by Spotnitz and Franklin [6], who considered an array of possible exothermic reactions and presented approaches for simulating a variety of abuse tests (oven, short-circuit, overcharge, nail, crush); this paper also contains an extensive review of experimental results. Yamauchi et al. [7] described an approach for simulating short-circuit behavior. Recently, Spotnitz et al. [11] described an approach for estimating the stability of packs when one cell goes into thermal runaway.

Abuse thermal behaviors of Li-ion batteries, especially large ones, have intrinsically three-dimensional features. Chen et al. presented three-dimensional thermal models for prismatic [12] and cylindrical [13] cells; these papers show that asymmetric temperature distributions arise from geometric effects and from

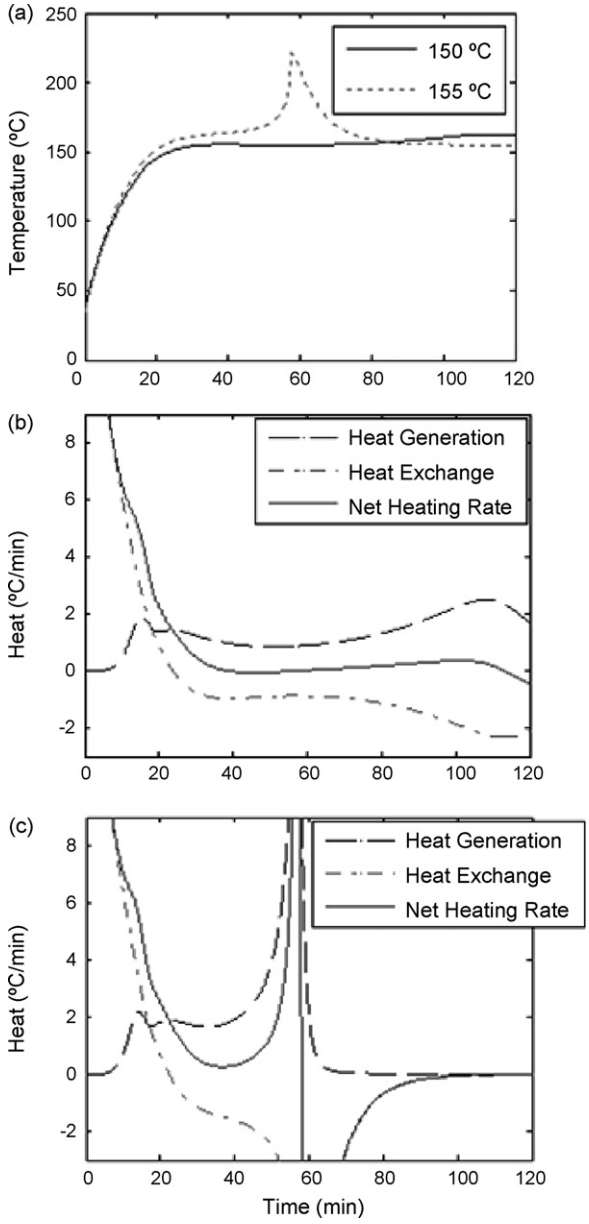

Fig. 2. Simulation of effect of oven temperature on thermal response of 18650 cell: (a) temperature vs. time; (b) heating rate terms for 150 °C oven; (c) heating rate terms for 155 °C oven.

convective heat transfer. Pesaran et al. [14] and Bharathan et al. [15] demonstrated the utility of three-dimensional models for improving the current and temperature distributions in batteries. However, these papers [12–15] did not consider abuse behaviors. Thermal abuse behaviors of Li-ion batteries are greatly affected by the local distributions of heat and materials. Therefore, three-dimensional modeling for capturing geometrical thermal effects on battery thermal abuse behavior is required. A three-dimensional model can capture the thermal paths inside a cell by addressing the geometries and properties of cell components [16]. Various thermal boundary conditions can be simulated for considering local cooling or heating effects. In addition, a three-dimensional analysis can address the effects of nonuniform distributions on heat release from the component reactions in a high-temperature environment.

To develop a three-dimensional thermal abuse model, we listed possible exothermic component reactions, and then implemented the abuse chemistry into the three-dimensional battery model. In this study, a commercial, finite-volume method software known as FLUENT® was used to develop the three-dimensional thermal abuse model for Li-ion batteries. The thermal abuse model does not explicitly consider internal short circuits that might occur during oven testing due to softening of the separator. However, localized heating of the cell is considered.

2.1. Energy balance

Thermal conduction is assumed to dominate internal heat transport in the system, which is true while the convective heat transfer through the net flow of electrolyte and production gas is limited. The temporal change of stored thermal energy in arbitrary control volume in the system equals to the difference between heat generation and net heat diffusion out, as shown in the following equation:

$$\frac{\partial(\rho c_p T)}{\partial t} = -\nabla(k\nabla T) + S,$$
$$S = S_{\text{abuse\_chem}} + S_{\text{joul}} + S_{\text{combustion}} + \cdots \quad (1)$$

where ρ (g cm^{-3}) is the density, c_p (J g^{-1} K^{-1}) the heat capacity, T (K) the temperature, t (s) the time, k (W cm^{-1} K^{-1}) the thermal conductivity, and S (W cm^{-3}) represents the heat source/sink terms. The volumetric heat generation that originated from Li-ion battery component reactions at increasing temperatures was listed in Eq. (2) and included in the three-dimensional battery thermal analysis:

$$S_{\text{abuse\_chem}} = S_{\text{sei}} + S_{\text{ne}} + S_{\text{pe}} + S_{\text{ele}} + S_{\text{nb}} \quad (2)$$

where S_{sei} is the heat from the SEI decomposition reaction, S_{ne} the reaction between the negative active material and electrolyte, S_{pe} the reaction between the positive active material and electrolyte, S_{ele} the electrolyte decomposition, and S_{nb} is the reaction between the negative active and binder.

One difficulty for the three-dimensional modeling of batteries is that extensive computational resources are needed to resolve the small-scale structures such as layered winding of electrodes, separators, and current collectors in a reasonable grid size. In this study, sub-grid scale structures are modeled as a continuous material with non-isotropic properties that depend on the layered directions of sub-grid structures. Orthotropic properties such as thermal conductivity of layered structure can be measured values, or can be evaluated with flux conservation relations through

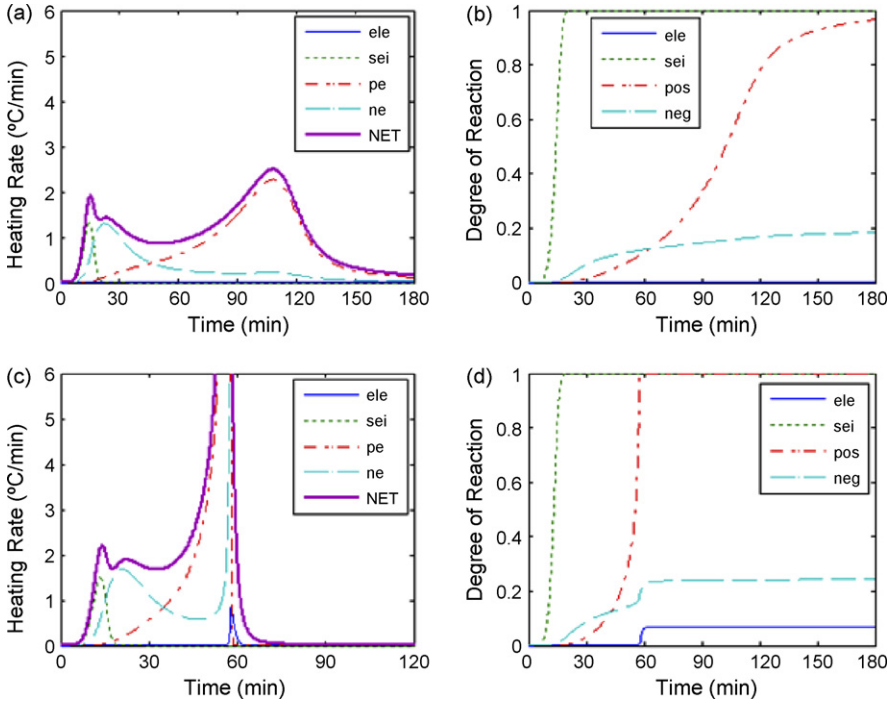

Fig. 3. Computed heating rate from the component reactions in simulated oven tests. 150 °C: (a) component terms, (b) degree of reaction; 155 °C: (c) component terms, (d) degree of reaction.

the layers and along the layers of thickness l_i (Eqs. (3) and (4)):

- Layer-normal direction:

$$k_n = \frac{\sum_i l_i}{\sum_i l_i / k_i} \tag{3}$$

- Layer-parallel direction:

$$k_p = \frac{\sum_i k_i l_i}{\sum_i l_i} \tag{4}$$

The heat exchange between the system and the ambient is computed through the thermal boundary conditions assigned at the computational domain boundaries. Combined thermal boundary conditions are applied to consider both the radiation and the convection heat transfer contributions at the cell surface. Convective heat flux out to ambient is evaluated in the following equation:

$$q''_{conv} = h(T_{surf} - T_{amb}) \tag{5}$$

where h is a convection heat transfer coefficient. For oven test simulations, Eq. (6) is used for radiative heat flux out to ambient from cell surface:

$$q''_{radi} = \varepsilon\sigma(T^4_{surf} - T^4_{amb}) \tag{6}$$

where ε is the emissivity of the cell surface and σ is the Stefan–Boltzmann constant. The oven chamber is assumed to be an isothermal cavity where the irradiation corresponds to emission from a blackbody, and the cell surfaces are considered as gray diffuse surfaces.

2.2. Thermal abuse reaction models

Li-ion battery thermal abuse reactions are modeled for three-dimensional battery simulation by listing component reactions that occur at elevated temperatures. Reactions involving lithium metal (which would be important in an overcharge test [6]) and combustion reactions are not considered in the current study, but the approach presented here could readily accommodate such reactions. Therefore, our model assumes that the flames are successfully prevented for the simulated cells that are not overcharged.

2.2.1. Solid electrolyte interface decomposition reaction

The negative electrode is protected from direct reaction with solvent by an ionically conducting film called the solid electrolyte interface (SEI). The layer is meta-stable and can decompose exothermically at 90–120 °C [17,18]. Following the formulation of Hatchard et al. [5], this reaction can be expressed in the following equations:

$$R_{sei}(T, c_{sei}) = A_{sei} \exp\left[-\frac{E_{a,sei}}{RT}\right] c_{sei}^{m_{sei}} \tag{7}$$

$$S_{sei} = H_{sei} W_c R_{sei} \tag{8}$$

$$\frac{dc_{sei}}{dt} = -R_{sei} \tag{9}$$

where c_{sei} is the dimensionless amount of lithium-containing meta-stable species in the SEI. R_{sei} (s^{-1}), A_{sei} (s^{-1}), $E_{a,sei}$ ($J\,mol^{-1}$) are reaction parameters. Specific heat release H_{sei} ($J\,g^{-1}$) is evaluated as Joule per gram of carbon, and W_c ($g\,m^{-3}$) is the volume-specific carbon content in the jellyroll.

2.2.2. Negative-solvent reaction

At elevated temperatures (>120 °C), an exothermic reaction between intercalated lithium and electrolyte can occur (Eqs.

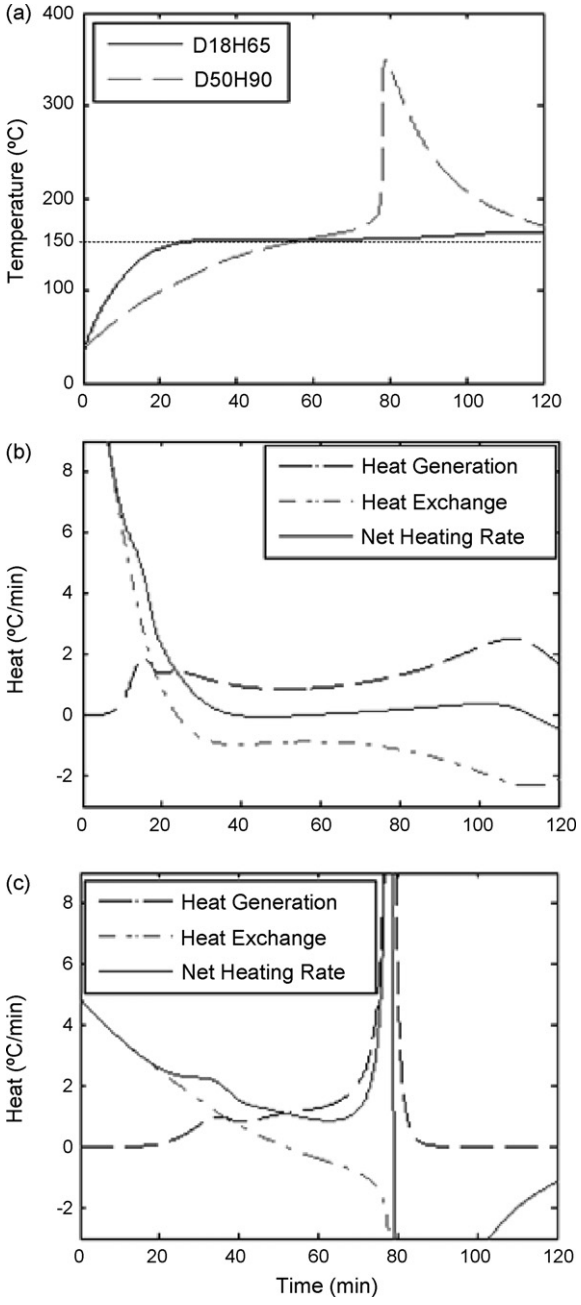

Fig. 4. Simulated effect of cell size in 150 °C oven test: (a) temperature vs. time; (b) component heat terms for D18H65 cell; (c) component terms for D50H90 cell.

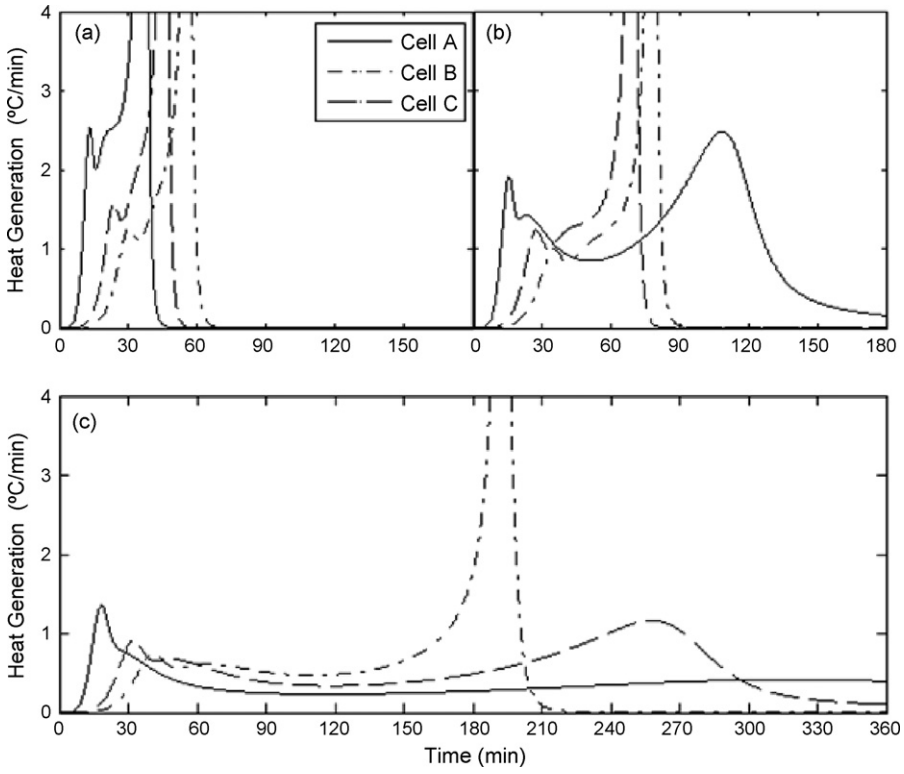

Fig. 5. Simulation of effect of cell size and surface:volume ratio (A/V_{jr}) on different temperature oven storing. (See Table 2, Cell A (A/V_{jr} = 48.57), Cell B (A/V_{jr} = 25.01), Cell C (A/V_{jr} = 29.14).): (a) 160 °C oven test; (b) 150 °C oven test; (c) 140 °C oven test.

(10)–(13)). Again, following the formulation of Hatchard et al. [5]:

$$R_{ne}(T, c_e, c_{neg}, t_{sei}) = A_{ne} \exp\left[-\frac{t_{sei}}{t_{sei,ref}}\right] c_{neg}^{m_{ne,n}} \exp\left[-\frac{E_{a,ne}}{RT}\right], \quad \text{tunneling regime} \tag{10}$$

$$R_{ne}(T, c_e, c_{neg}, t_{sei}) = A_{ne} \left(\frac{t_{sei,ref}}{t_{sei}}\right) c_{neg}^{m_{ne,n}} \exp\left[-\frac{E_{a,ne}}{RT}\right], \quad \text{diffusion regime} \tag{11}$$

$$S_{ne} = H_{ne} W_c R_{ne} \tag{12}$$

$$\frac{dc_{neg}}{dt} = -R_{ne} \tag{13}$$

where c_{neg} is the dimensionless amount of lithium intercalated within the carbon; t_{sei} a dimensionless measure of SEI layer thickness that reflects the amount of lithium in the SEI; and R_{ne} (s^{-1}), A_{ne} (s^{-1}), $E_{a,ne}$ (J mol^{-1}) are the reaction parameters. Specific heat release H_{ne} (J g^{-1}) is evaluated as Joule per gram of carbon, and W_c (g m^{-3}) is the volume-specific carbon content in the jellyroll.

Table 2
Cell sizes and surface:volume ratios (A/V_{jr}) used for oven test simulations

	Cell A	Cell B	Cell C
V_{jr} (cm^3)	10.52	157.1	157.1
A/V_{jr} (m^{-1})	48.37	25.01	29.14

2.2.3. Positive-solvent reaction

In the oxidized state, the positive material reacts directly with the electrolyte. Or, the positive active material can decompose exothermically and emit oxygen that can react exothermically with the electrolyte. In any case, the chemical reduction of the positive active material with the electrolyte is highly exothermic

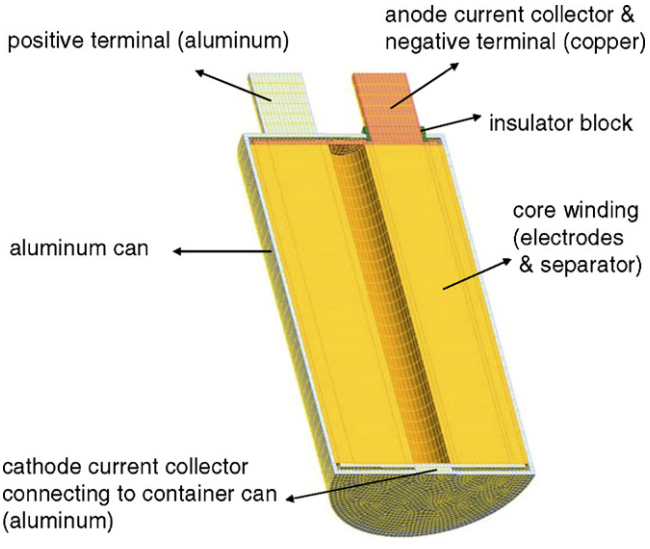

Fig. 6. Schematic of model geometry and a computational mesh.

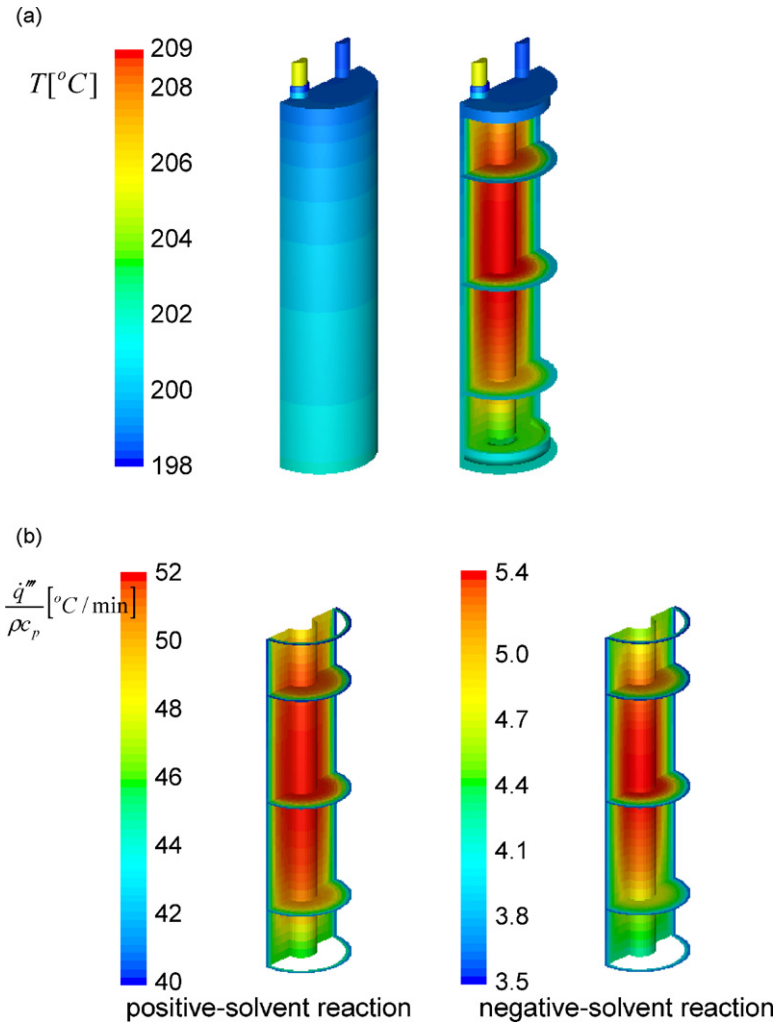

Fig. 7. Three-dimensional simulation of 155 °C oven test for a 18650 cell: (a) temperature distribution at 55 min; (b) heat generation for positive-solvent and negative-solvent reactions at 55 min.

(Eqs. (14)–(16)). Following the formulation of Hatchard et al. [5]:

$$R_{pe}(T, \alpha, c_e) = A_{pe}\alpha^{m_{pe,p1}}(1-\alpha)^{m_{pe,p2}} \exp\left[-\frac{E_{a,pe}}{RT}\right] \quad (14)$$

$$S_{pe} = H_{pe} W_p R_{pe} \quad (15)$$

$$\frac{d\alpha}{dt} = R_{pe} \quad (16)$$

where α is the degree of conversion. R_{pe} (s^{-1}), A_{pe} (s^{-1}), $E_{a,Pe}$ ($J\,mol^{-1}$) are reaction parameters. Specific heat release H_{pe} ($J\,g^{-1}$) is evaluated as Joule per gram of positive-active content, and W_p ($g\,m^{-3}$) is the volume-specific, positive-active content in the jellyroll.

2.2.4. Electrolyte decomposition reaction

The electrolyte can decompose exothermically at elevated temperatures (>200 °C), as expressed in the following equations:

$$R_e(T, c_e) = A_e \exp\left[-\frac{E_{a,e}}{RT}\right] c_e^{m_e} \quad (17)$$

$$S_{ele} = H_e W_e R_e \quad (18)$$

$$\frac{dc_e}{dt} = -R_e \quad (19)$$

where c_e is the dimensionless concentration of electrolyte and R_e (s^{-1}), A_e (s^{-1}), $E_{a,e}$ ($J\,mol^{-1}$) are the reaction parameters. Note that k_e is a frequency factor rather than a rate constant. Specific heat release H_e ($J\,g^{-1}$) is evaluated as Joule per gram of electrolyte, and W_e ($g\,m^{-3}$) is the volume-specific electrolyte content in the jellyroll.

2.3. Model verification

We verified the chemistry portion of the three-dimensional implementation by comparing a simple lumped[1] thermal model with the one-dimensional results presented by Hatchard et al. [5]. The chemistry portion of the model reproduced the results of

[1] The term "lumped model" indicates that internal temperature gradients are relatively small so that a single temperature can be used for the entire model domain.

Hatchard et al. [5], with small differences caused by the lumped versus one-dimensional treatment (Fig. 1).

3. Results

The model parameters used in this study were collected from the literature. Open information is limited, but Table 1 presents the values of model parameters used to describe the $LiCoO_2$/graphite chemistry at full charge. The lumped model results were used to investigate the effects of cell size and oven temperature on the thermal abuse behavior of a cell under the oven test. Three-dimensional oven test simulation results are presented to address the impact of temperature nonuniformity and material distributions through a cell. The three-dimensional model was used to simulate a localized heat release and the propagation of the chemical reactions inside a cell.

3.1. Lumped model-oven test simulation

Oven test simulations were carried out with the lumped model to investigate the impact of oven temperature and cell size. The cells and batteries were assumed to be initially at a normal operating temperature (35 °C), and then suddenly placed in an oven that was preheated to the desired test temperature. The oven temperature was kept constant during the test. Natural convection and radiative heat transfer were considered at the cell surface ($h = 7.17\ W\ m^{-2}\ K$, $\varepsilon = 0.8$).

We examined the effect of oven temperature on the thermal behavior of an 18650-size cell (cylinder, 18 mm diameter, 65 mm height) for two oven temperatures; 150 and 155 °C. We introduced thermal mass-specific heating rates, Q/Mc_p (°C min^{-1}) to quantify the internal heat generation and heat exchange with ambient. Fig. 2(a) shows the cell temperature variations for both oven temperature cases. Internal heat generation that resulted from thermal abuse reactions and heat transferred from ambient were plotted with the sum of both contributions for each oven temperature in Fig. 2(b) and (c), respectively. The cell placed in the 150 °C oven did not go into thermal runaway; the cell heating in the oven at 155 °C did go into thermal runaway. The initial heating rate profiles are similar in both oven temperature cases. The initial heating rates ($t < 20$ min) were determined mainly by the heat transfer from ambient.

In the 150 °C oven heating case, heat generation and heat rejection came to balance at about 40 min. The net heating rate increased gradually afterward as the reactions slowly went on until about 110 min when the reactants were depleted. On the other hand, in the 155 °C case, the heat generation rate rapidly increased to exceed the heat rejection to ambient at around 50 min and led to thermal runaway.

To better understand the effect of oven temperature, the heat release by each component was closely examined. Heat generation from each component reaction was quantified and plotted along with the net heat generation for the 150 °C oven temperature case in Fig. 3(a). Time variations of reaction degree of the component reactions are shown in Fig. 3(b). Fig. 3(c) and (d) presents the same quantities for the 155 °C oven temperature case. In the initial heating period ($t < 15$ min), the SEI decomposition reaction contributed the most to total heat generation in both temperature cases to show the first local maximum. This heat was released between 80 and 140 °C and was mostly used to heat the cell. At 20 min $< t <$ 30 min, the negative-solvent reaction led to total heat generation. The reaction slowed as the diffusion thickness for reacting Li-ion in the negative particles increased. The positive-solvent reaction was autocatalytic [19]; that is, the reaction initially proceeded slowly but accelerated rapidly as reaction products that promoted the reaction were formed. Positive-solvent reaction heat release increased gradually and dominated the total heating rate at $t > 60$ min in

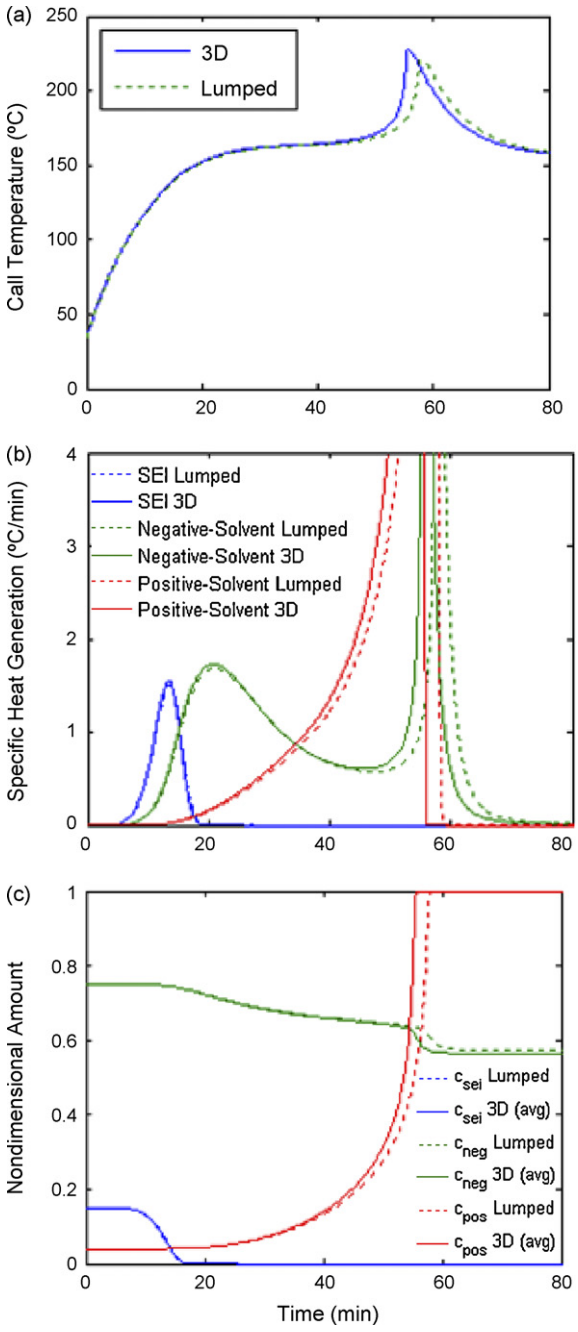

Fig. 8. Comparison of three-dimensional and lumped model results for 155 °C oven test of a 18650 cell: (a) temperature; (b) heat generation of component reactions; (c) reaction quantity.

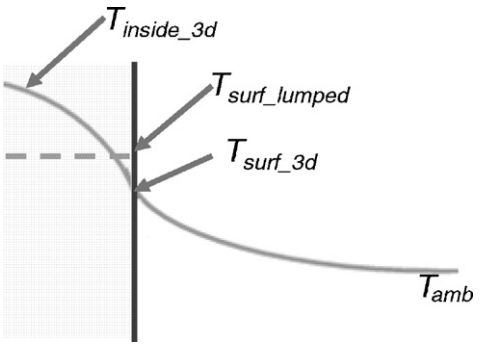

Fig. 9. Schematic of temperature gradients computed from lumped and three-dimensional models.

the 150 °C oven heating case, and at $t > 40$ min in the 155 °C oven heating case. In the 155 °C case, a sudden temperature increase (at about 60 min) caused by the positive-solvent reaction enhanced the negative-solvent reaction again and triggered the electrolyte decomposition. But the reaction ceased after cool-down to ambient temperature. In the 150 °C case, internal heat generation occurred slowly enough for the generated heat to be rejected to ambient without thermal runaway.

The effect of a cell's size on its thermal behavior was investigated for a fixed oven temperature. A small cell (D18H65, 18 mm diameter and 65 mm height) and a large cell (D50H90, 50 mm diameter and 90 mm height) were simulated for 150 °C oven temperature heating. Fig. 4(a) shows the cell temperature variations for the both size cell cases. Internal heat generation caused by thermal abuse reactions and heat transferred from ambient was plotted with the sum of both contributions for each size of cell, as shown in Fig. 4(b) and (c), respectively.

The rate of temperature rise was initially much slower in a large cell than in a small cell because the volume-specific heat exchange area was smaller in the large cell. So, the small cell heated rapidly but stayed at slightly higher temperature than the oven temperature while the exothermic reactions slowly occurred. In the small cell case, heat rejection to ambient balanced with heat generation so thermal runaway was averted. In the larger cell (D50H90), heat generation started slowly but increased continuously. Heat rejection started much later (about 50 min) in the larger cell and the magnitude of rejection heat was relatively small compared to heat generation, which led to thermal runaway.

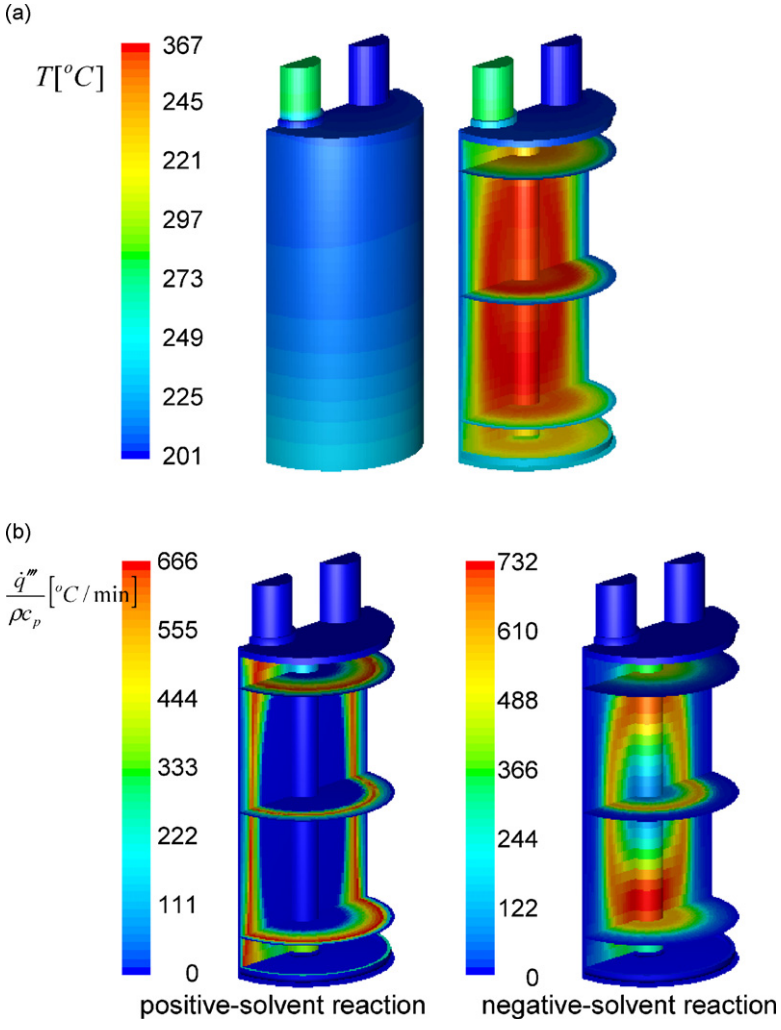

Fig. 10. Simulation of 155 °C oven test for D50H90 cell using three-dimensional model.

Heat generation rates per cell thermal mass are plotted in Fig. 5 for the oven heating time at three oven temperatures with three cells. Table 2 presents the jellyroll volumes and volume-specific heat transfer areas for the tested cells. Cell A and Cell B represent D18H65 and D50H90 size cylindrical cells, respectively; Cell C represents a cell that has same volume with D50H90 cell but a different form factor to have a larger heat exchange surface. The number for the volume-specific surface area of Cell C was calculated from an elliptical cylinder cell.

Heat exchange surface area per jellyroll volume, A/V_{jr}, is a critical factor for determining initial heating and heat dissipation to ambient. On the other hand, the heat generation rate is sensitive to the cell temperature. For larger A/V_{jr}, the cell leads to thermal runaway faster at high oven temperature (160 °C), but the heat rejection is large enough to balance with the heat generation at low oven temperature (140 °C) so thermal runaway can be avoided. The result implies that increasing A/V_{jr} lowers the onset oven temperature, which triggers the cell thermal runaway, and large A/V_{jr} shortens the time for oven heating to make the cell undergo thermal runaway, if it occurs.

3.2. Three-dimensional, lithium-ion thermal abuse model

We used the model based on finite-volume methods to conduct three-dimensional thermal abuse simulations for Li-ion batteries. The parameters for atypical fully charged $LiCoO_2$/graphite chemistry were used (see Table 1). Fig. 6 shows a schematic of a sample model geometry and computational mesh used in the simulations. One-half model with symmetry surface was used. The total number of computational cells in the meshes is about 42,000. The computational cells are hexahedral and ranged in volume from 3.13E−10 to 5.44E−9 m^3. The model geometry includes the cell component details such as aluminum/copper current collectors and terminals, insulator blocks, aluminum container, and cell core winding. We addressed the material property variations in the continuous calculation domain by dividing the domain into several computational zones. For the cells studied here, the container can is electrically and thermally connected to one of the terminals (Fig. 6). NREL's Linux cluster was used for the three-dimensional computations.

3.2.1. Three-dimensional oven test simulation

Even though the oven test is not a conspicuous case in which the three-dimensional effects are critical, 155 °C oven test cases for the different size cells were simulated three dimensionally, and the results were compared with the lumped analysis results to see the impact of nonuniform distributions. The model incorporates the heat released from the component reactions, SEI decomposition, negative-solvent reaction, positive-solvent reaction, and electrolyte decomposition reaction. The thermal boundary condition for the cell exterior surface addresses natural convection and radiation heat exchange ($h = 7.17\ W\ m^{-2}\ K$, $\varepsilon = 0.8$). Black-body irradiation and gray surface conditions were assumed.

Fig. 7 presents the contours of temperature and heat generation for the D18H65 small size cell oven test after storing at 155 °C for 3300 s. At the specified time, the cell undergoes thermal runaway. The highest temperature appears at the cell center where the chemical reactions are stronger. The temperature gradient is larger in the layer normal (radial) direction. A larger temperature gradient does not directly mean larger heat flux because of the nonisotropic thermal conductivity of the cell core. The bottom of the cell core winding is thermally connected to the can through the current collector. So, the lower section of the core is cooled better and results in lower temperature and heat generation than the upper section.

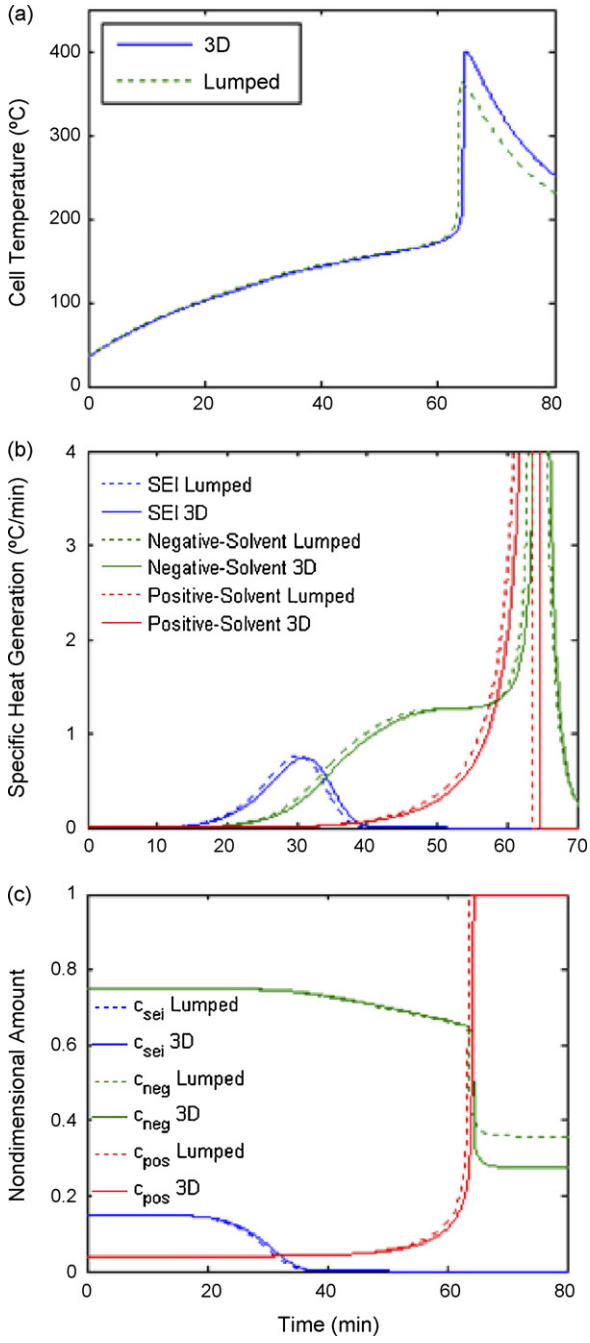

Fig. 11. Comparison of lumped and three-dimensional models for 155 °C oven test of a D50H90 cell: (a) temperature; (b) heat generation of component reactions; (c) reaction quantity.

The temporal variations of three-dimensional model cell average values for temperature, heat generation, and reaction parameters were compared with the lumped analysis quantity variations in Fig. 8 for the D18H65 cell. Nonuniform distribution affects the results in two aspects: (1) heat exchange between the cell and ambient environment is more accurately calculated by capturing the local temperature profiles at the surface and (2) the spatial variation of temperature and the local reaction parameters are captured so the chemical reaction rates that are susceptive to local variables can be evaluated more accurately. As shown in Fig. 8, the three-dimensional simulation results are generally matched with the lumped system analysis, but the start of thermal runaway is moved up by several minutes. Because of the (relatively) large A/V_{jr} of D18H65, the cell heats rapidly and starts to reject heat to ambient at about 20 min. During the heat rejection period, the captured temperature profiles in the three-dimensional model make the heat rejection rates at the cell's surface be lower, and reaction rates at the cell's inner core region are higher than in the lumped system analysis (Fig. 9). So, the thermal runaway is advanced by several minutes in the three-dimensional simulation compared to the lumped analysis case.

Fig. 10 presents the contours of temperature and heat generation for the D50H90 size cell oven test after storage at 155 °C for 3860 s. At the specified time, the cell undergoes thermal runaway. Spatial distribution nonuniformity is more apparent than with the D18H65 case. The highest temperature appears at core center region. The reactants of positive-solvent reaction are already depleted at the center region of the cell so that the reaction occurs only in the outer rim and at both ends (near the top and bottom) of the winding at the specified time. Since the heat generation rate is much larger than the surface heat rejection rate, temperature distribution is dominated by the heat generation rather than by the location of heat transfer surfaces.

We examined the nonuniform distribution effects in the larger cell oven test case by comparing the averaged values from the three-dimensional model results with the lumped model results (Fig. 11). The three-dimensional simulation results generally matched with the lumped system analysis. But, the start of thermal runaway was delayed by a few minutes and the maximum temperature was higher. Due to the (relatively) small A/V_{jr} of D50H90, the cell heated slowly and did not reject heat to ambient until about 50 min. (Thermal runaway occurs at about 65 min.) During the long heat absorption period (0 min< t < 50 min), capturing the distributions in the three-dimensional model results in the lower rate of heat absorption from ambient at the surface and lower reaction rates at the inner core region. So, the thermal runaway appears to be delayed by a few minutes compared with the lumped model case. Due to the definite nonuniform distribution of temperature (the much higher than average temperature inside a cell), negative-solvent reaction progresses further on average so that the total heat release is greater to increase the maximum average cell temperature in the three-dimensional simulation case than in the lumped system analysis case.

A sequence of component heat generation contours for the D50H90 size cell oven test simulation is presented in Fig. 12. The SEI decomposition reaction occurs much earlier (15–40 min) than the thermal runaway. Therefore, only the heat releases of positive-solvent and negative-solvent reactions are presented here.

3.2.2. *Localized heating simulation*

The three-dimensional model was used to simulate a localized heating event (such as an internal short circuit) to investigate the thermal abuse reaction propagation inside a D50H90 cell. A three-dimensional model is essential for simulating a localized heating event that is intrinsically multidimensional. A half-cell model with a symmetry plane was introduced. Internal hot spots

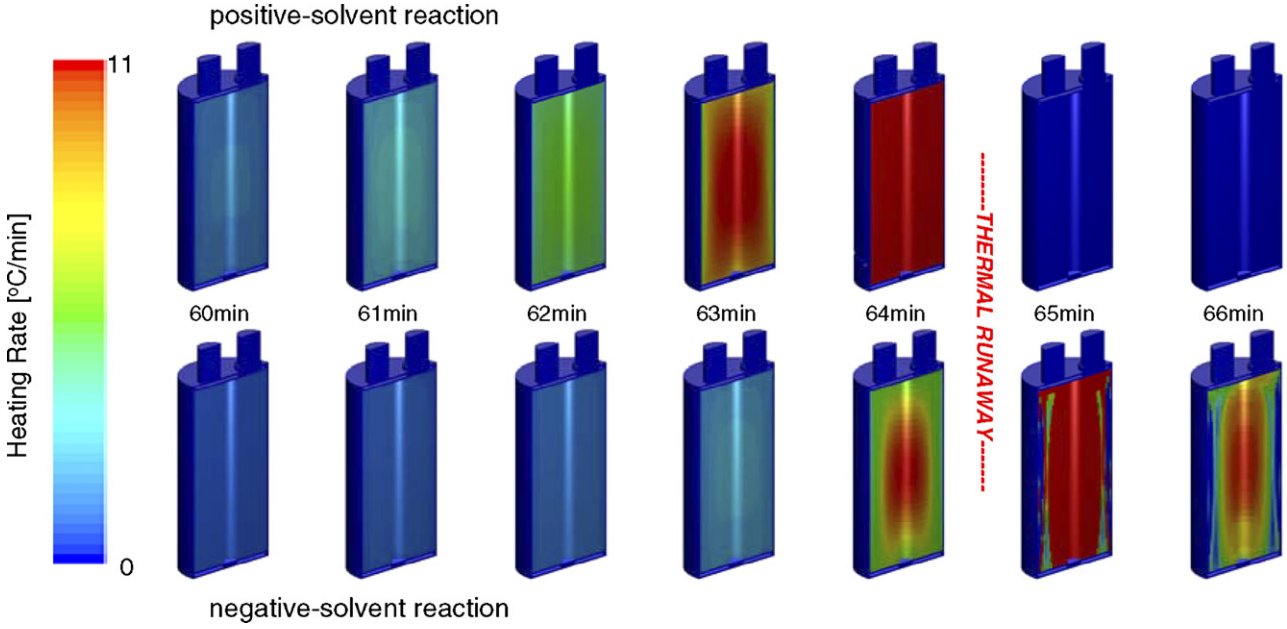

Fig. 12. Simulated sequence of component heat generation contours for a D50H90 cell in a 155 °C oven test using three-dimensional model.

were modeled by releasing localized energy in a short time in a very small region inside the cell core. Boundary conditions were also localized. Each boundary section can have various boundary conditions independently. In the following case, a specified amount of energy (here equivalent to 15% of stored energy in the cell) is released in a small portion of core volume (0.5% of total jellyroll volume) for 1 s. Initial temperature of the cell was 55 °C. The cell was assumed to be cooled at the side surface with a heat transfer coefficient $h = 5\ \mathrm{W\ m^{-2}\ K}$ and ambient temperature $T_{amb} = 35\ ^{\circ}\mathrm{C}$.

Fig. 13 shows the spatial distributions of temperature and heat generation, and the shape of a reaction surface at 6 s after the initial local heat release at the middle of the cell winding. The temperature contour presented in Fig. 13(a) shows that the initial hot temperature region mainly expands in the azimuthal and longitudinal directions. The initial reaction front propagating directions are more clearly seen in heat generation contours in Fig. 13(b).

The pattern of thermal abuse reaction propagation following the initial local spot heating at the middle of the cell core winding was investigated. The temporal variations of cell average temperature and total heat release are plotted in Fig. 14. During the propagation of the abuse reactions through the cell, we observed several propagating stages where the cell average heat release rate increases suddenly. The corresponding temperature contours were produced and shown in Fig. 14.

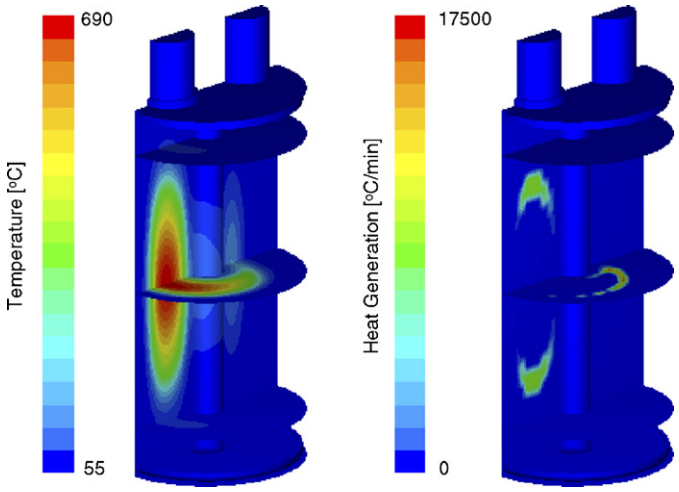

Fig. 13. Computed spatial distributions of temperature and heat generation at 6 s after the initial local heat release.

(1) *Initial propagation*: In the beginning, the thermal abuse reactions propagate in the azimuthal and longitudinal directions from the reaction ignition spot so that the reaction zone forms a hollow cylindrical shape.
(2) *Reaction at the core axis*: Since the internal temperature distribution largely depends on conduction heat transfer at this stage, the highest temperature appears at geometric center of the cell. As reactions and heat transport go on, the center

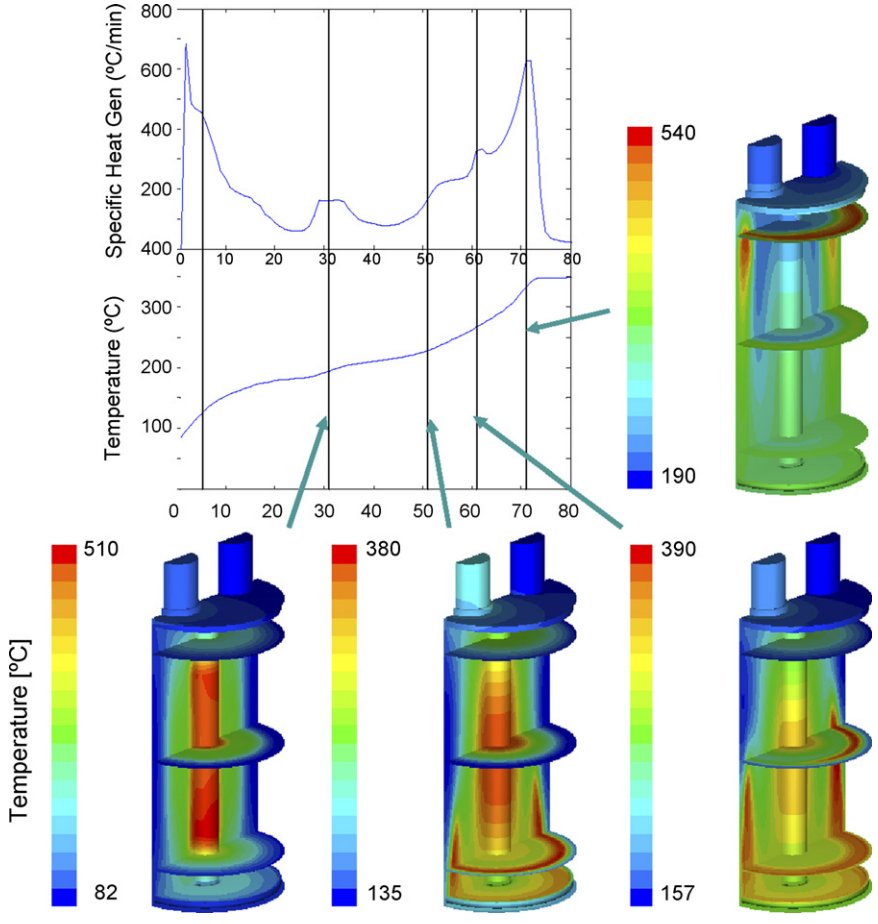

Fig. 14. Simulated pattern of reaction propagation due to local heating.

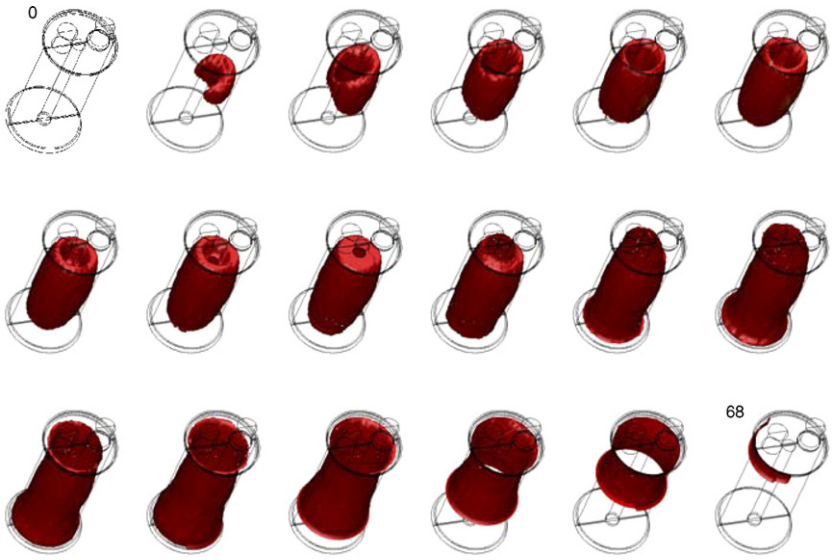

Fig. 15. Simulated iso-surface contours of SEI decomposition reaction propagation due to local heating. The shown numbers are time after the initial localized heat release. Each frame is 4 s apart.

of the cell starts to react and the reactions propagate along the cell axis where the nonreacted materials remain.

(3) *Reaction through the outer rim*: As the cell is continuously heated, the outer rim of the cell is taken to the reaction from bottom to top. Since the container can is thermally connected to the bottom of the jellyroll, the bottom section of the cell is close to the thermal center, and heats sooner than the top section of the cell.

The thermal abuse reaction propagation is more clearly seen at the consecutive iso-surface contours by presenting a sequence of SEI decomposition reaction completion surface (see Fig. 15).

4. Conclusion

Chemical reactions at elevated temperatures in Li-ion batteries were listed and formulated to be included in a three-dimensional Li-ion battery thermal abuse model. Reaction chemistry was implemented into a three-dimensional, finite-volume method battery model that addresses the effects of nonuniform distributions, thermal and electrical path design inside cells, localized heating and cooling, and cell component geometry and materials. Oven simulation indicates that cell size (or more precisely, heat transfer area per unit volume) greatly affects the thermal behavior of a cell in an oven test. Nonuniform distribution effects were captured in the three-dimensional battery simulation. A localized heat release (representing a short circuit) was simulated, and the results were visualized to show the cell-internal propagation of the abuse reactions. The reactions initially propagate in the azimuthal and longitudinal directions to form a hollow cylinder-shaped reaction zone. Then the heat accumulation causes the center core of the cell to react. Finally, the reaction propagates to the outer rim of the cell.

This study describes the development of a three-dimensional-capable thermal abuse model for lithium-ion cells and successfully demonstrates multidimensional behaviors of thermally abused cells. Future work will include expanding the model to address various chemistries and cell-to-cell abuse reaction propagation in a multistring module.

Acknowledgments

The U.S. Department of Energy (DOE), Office of Energy Efficiency and Renewable Energy funded this effort. We appreciate the support provided by Dave Howell and Tien Duong, DOE Program Managers at the Office of the Freedom CAR and Vehicle Technologies.

References

[1] G. Venugopal, J. Power Sources 101 (2001) 231.
[2] P.G. Balakrishnan, R. Ramesh, T.P. Kumar, J. Power Sources 155 (2006) 401.
[3] G.G. Botte, B.A. Johnson, R.E. White, J. Electrochem. Soc. 146 (1999) 914.
[4] T.D. Hatchard, D.D. MacNeil, D.A. Stevens, L. Christensen, J.R. Dahn, Electrochem. Solid-State Lett. 3 (2000) 305.
[5] T.D. Hatchard, D.D. MacNeil, A. Basu, J.R. Dahn, J. Electrochem. Soc. 148 (7) (2001) A755–A761.
[6] R. Spotnitz, J. Franklin, J. Power Sources 113 (2003) 81.
[7] T. Yamauchi, K. Mizushima, Y. Satoh, S. Yamada, J. Power Sources 136 (2004) 99.
[8] S.A. Hallaj, H. Maleki, J.S. Hong, J.R. Selman, J. Power Sources 83 (1999) 1.
[9] C M. Doyle, Chemical Engineering, PhD, University of California, Berkeley, 1995.
[10] M.N. Richard, J.R. Dahn, J. Power Sources 79 (1999) 135.
[11] R.M. Spotnitz, J. Weaver, G. Yeduvaka, D.H. Doughty, E.P. Roth, J. Power Sources 163 (2007).
[12] S.C. Chen, C.C. Wan, Y.Y. Wang, J. Power Sources 140 (2005)111.
[13] S.C. Chen, Y.Y. Wang, C.C. Wan, J. Electrochem. Soc. 153 (2006) A637.
[14] A. Pesaran, D. Bharathan, G.-H. Kim, A. Vlahinos, T. Duong, Proceedings of the 21st Electric Vehicle Symposium, Monte Carlo, Monaco, 2005.

[15] D. Bharathan, A. Pesaran, G.-H. Kim, A. Vlahinos, Proceedings of the IEEE Vehicle Power and Propulsion Conference IEEE, Chicago, IL, USA, 2005.
[16] A.A. Pesaran, J. Power Sources 110 (2002) 377.
[17] M.N. Richard, J.R. Dahn, J. Electrochem. Soc. 146 (1999) 2068.
[18] M.N. Richard, J.R. Dahn, J. Electrochem. Soc. 146 (1999) 2978.
[19] D.D. MacNeil, J.R. Dahn, J. Electrochem. Soc. 148 (2001) A1205.
[20] C. Lampe-Onnerud, J. Shi, R. Chamberlain, P. Onnerud, Proceedings of the 16th Annual Battery Conference on Applications and Advances, IEEE, Long Beach, CA, USA, 2001, p. 367.